AIAA JOURNAL
Vol. 41, No. 11, November 2003

Thermal Regime of Catalyst Particles in Reactor for Production of Carbon Nanotubes

Alex Povitsky*
University of Akron, Akron, Ohio 44325-3903
and
Manuel D. Salas†
NASA Langley Research Center, Hampton, Virginia 23681-2199

This study was motivated by an attempt to optimize the high-pressure carbon oxide process for the production of carbon nanotubes from gaseous carbon oxide. The goal is to achieve rapid and uniform heating of catalyst particles by an optimal arrangement of jets. A mixed Eulerian and Lagrangian approach is implemented to track the temperature of catalyst particles along their trajectories as a function of time. The poor performance of the original reactor configuration is explained in terms of features of particle trajectories. The trajectories most exposed to the hot jets appear to be the most problematic for heating because they either bend toward the cold-jet interior or rotate upwind of the mixing zone. To reduce undesirable slow and/or oscillatory heating of catalyst particles, a reactor configuration with three central jets is proposed, and the optimal location of the central and peripheral nozzles is determined.

Nomenclature

k	=	turbulent kinetic energy
Re	=	Reynolds number
R_ϕ	=	residual for variable ϕ
r_p	=	peripheral nozzle radius
r_0	=	central nozzle radius
T	=	temperature of gas
t_L	=	fluid Lagrangian integral time
y^*	=	nondimensional distance from the reactor wall
z	=	axial coordinate
α	=	angle between the central and a peripheral jets
β	=	angular location of initial coordinate of catalyst particle
ϵ	=	dissipation rate of turbulent energy

I. Introduction

THE goal of this study is to develop a computational approach to evaluate mixing of flow fluxes in a temporal scale. This approach is applied to optimization of reactor for production of carbon nanotubes.

Usually, in chemical and energy engineering, the rate of mixing of reagents in a reactor is estimated as a function of a spatial coordinate, for example, as the completeness of mixing in cross sections along the reactor axis. To evaluate the quality of mixing in a spatial scale, the system of Navier–Stokes equations together with an appropriate model of turbulence were solved using an Eulerian approach.[1–4] This approach was used by the first author's preliminary study[5] to show that for fast jet mixing in a spatial scale a high angle of incidence between jets is advantageous. However, a short spatial scale does not necessarily imply rapid and monotonic heating of the catalyst particles in temporal scale.

In this study the proposed way to evaluate particle trajectories is applied to improve the performance of the high-pressure carbon oxide process (HiPco) used for production of carbon nanotubes from gaseous carbon oxide.[6]

Perhaps the most significant spinoff product of fullerene research is the carbon nanotube, discovered by Iijima[7] in 1991. Nanotubes are carbon sheets seamlessly wrapped into cylinders with the ends capped by half-fullerenes. The tubes are only a few nanometers in diameter, but (with today's technology) up to a millimeter long; hence, the length-to-width aspect ratio is extremely high. The tubes can have single walls or multiwalls; the latter are more common and can be produced in bulk.

Single and multiwall nanotubes are interesting nanoscale materials for aerospace applications for three reasons.

A single-wall nanotube can be either metallic or semiconducting, depending on how exactly the hexagons forming the sheet line up. In addition, it is also possible to connect two nanotubes with different electrical properties. Quasi-one-dimensional heterojunctions, including metal–metal and metal–semiconductor, can, thus, be created, resulting in nanoscale electronic components.[8] These nanotube heterojunctions with electronic switching properties can be used for developing next generations of computer components.

Single and multiwall nanotubes have very good elastomechanical properties, thus, they have great potential for spacecraft components requiring lightweight, highly elastic, and very strong fibrous material.[9]

Because nanotubes are hollow, tubular, caged molecules, they have been proposed as lightweight packing material for hydrocarbon fuels, as nanoscale containers for molecular drug delivery, and as casting structures for making metallic nanowires and nanocapsulates.[10]

In the HiPco process, the catalyst particles $Fe(CO)_5$ initialize formation of carbon nanotubes from carbon oxide. The catalyst particles enter the HiPco reactor at room temperature and are heated up to 1000°C in the reactor. To avoid formation of Fe clusters, which do not act as a good catalysts, the catalyst particles should be heated as quickly as possible. In the current reactor design, hot peripheral jets are used to heat the cold central jet that carries the catalyst particles (Fig. 1). The gas in the central jet and peripheral jets is high-pressure CO. The goal of this study is to increase the mixing rate between jets in such a way as to maximize the heating rate of catalyst particles. Three types of particle trajectories will be discussed in the current study (Fig. 2). Trajectory 1 bends inward in the central jet, trajectory 2 is a representative of trajectories that bend outward, and trajectory

Received 13 March 2001; accepted for publication 12 September 2002.

*Associate Professor, Department of Mechanical Engineering; povitsky@uakron.edu. Member AIAA.

†Director, ICASE; currently Senior Scientist, Aerospace Vehicle Systems Technology Office, Mail Stop 254; manuel.d.salas@nasa.gov. Senior Member AIAA.

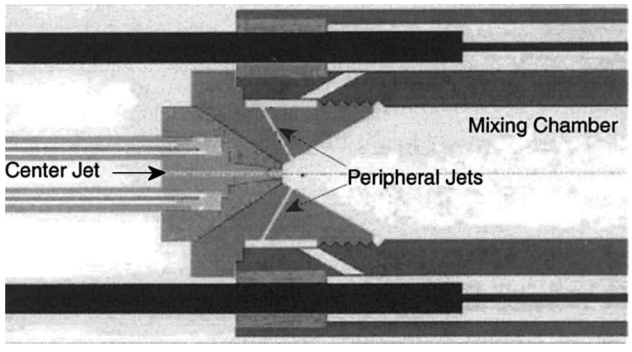

Fig. 1 HiPco reactor; cold central jet issues through the bottom; hot peripheral jets issue through side walls and meet at the centerline.

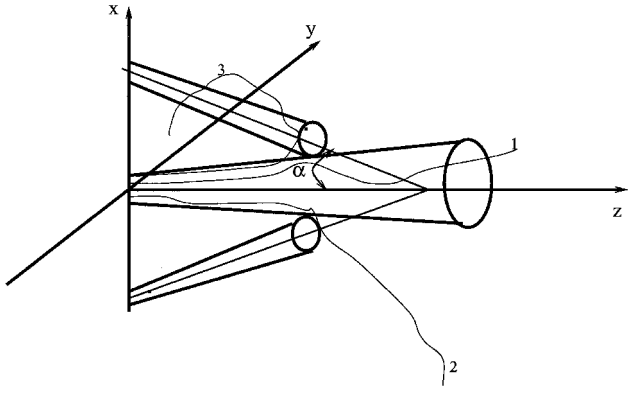

Fig. 2 Behavior of trajectories for high-incidence jet mixing: 1) trajectory bends inward, 2) trajectory bends outward, and 3) rotating trajectory.

3 belongs to trajectories involved in the vortex formed upstream of the intersection of the jets (Fig. 2).

It is shown here that, at the high angle of incidence between mixing jets, the particle trajectories may either be bent substantially toward the cold-jet interior or recirculate upstream of the jet intersection. This leads to a dramatic reduction of heating rate and to large oscillations of particle temperature. The computation of particle trajectories (also known as the Lagrangian approach) provides the explicit temporal evolution of the particle temperature. In this study, the computed temporal temperature profiles of the catalyst particles are used to find the optimal configuration of mixing jets.

The bending and rotation of trajectories, especially those that are mostly exposed to the hot jets and are, therefore, supposed to heat up well cannot be avoided by simple procedures such as increasing the hot-to-cold jet mass ratio, increasing the angle between jets, and splitting the cold jet.

A special configuration of cold and hot jets that avoids direct exposure of the cold jet and provides roughly three times larger heating rate than the basic design is proposed and modeled here.

In Sec. II, the design of the HiPCo reactor and its operation is described. In Sec. III, the adopted mathematical model, implemented numerical methods, and the grid generation features are discussed in terms of the capabilities of the FLUENT computational fluid dynamics software[11] used in this study. In Sec. IV, the results of the reactor modeling are discussed. In Sec. V, a novel configuration of nozzles is proposed, and the results of modeling are compared with those for the basic reactor. In this section, the stochastic effect of turbulent jet mixing on particle trajectories will be discussed.

II. Description of the HiPco Reactor

The basic configuration of the reactor is used in the study.[12] The cold jet issues into the reactor working space through the central nozzle with $r_0 = 0.5$ mm nozzle radius. The cone/cylinder working space of the reactor includes coaxial funnel ($L_f = 36r_0$, $R_1 = 4.35r_0$, and $R_2 = 21.25r_0$) and cylindrical parts ($L_c = 75r_0$ and $R = R_2$) (Fig. 3).

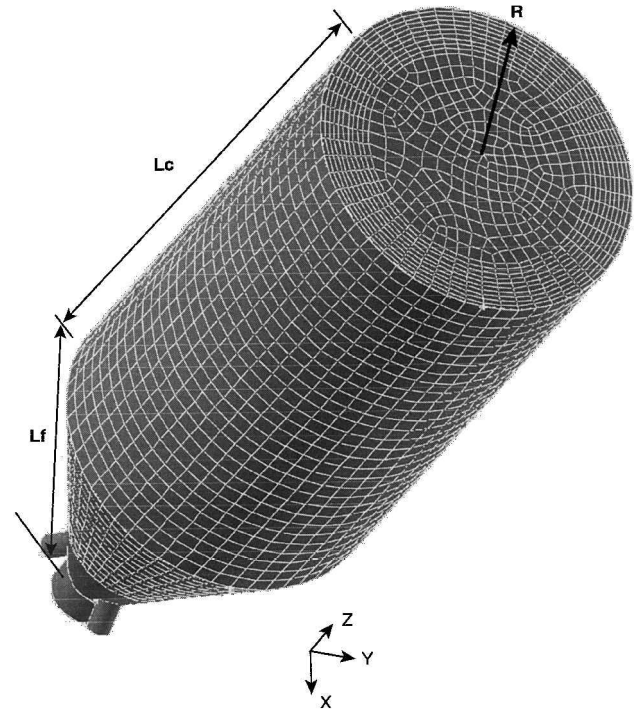

Fig. 3 Computational volume and numerical grid.

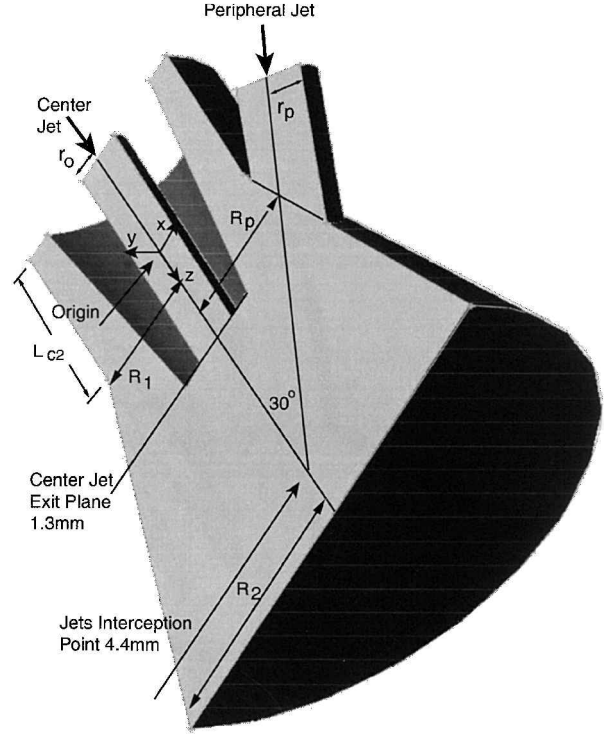

Fig. 4 Showerhead of the reactor.

A smaller cylinder ($R = R_1$ and $L_{c2} = 5r_0$) is coaxial with the funnel and surrounds the central nozzle (Fig. 4). The center of the smaller basis of the funnel is located at the origin (Fig. 4).

The central jet exit is located on the centerline, $z = 1.3$ mm. The cold jet has a temperature of 373 K and a flow velocity of 37 m/s. Each hot jet exits through a peripheral nozzle with a 1.5-mm nozzle diameter after being heated to 1323 K. For a 1:3 mass ratio of central to peripheral jets, the peripheral jet velocity is 59 m/s. The reactor wall is heated to 1373 K.

The centers of the peripheral nozzles (with radius $r_p = 1.5r_0$) are located at the reactor funnel, $z = 1$ mm and local funnel radius

$R_p = 2.65$ mm (Fig. 4). The jets are oriented so that the central and peripheral jets intersect at a point located at the reactor centerline. If the angle between the cold and peripheral jets is 30 deg, this intersection point is located at distance 3.1 mm from the central jet exit and 4.3 mm from a peripheral jet exit.

III. Mathematical Model, Numerical Method, Grid and Geometry Generation

A. Computational Volume and Numerical Grid Generation

The computational volume and numerical grid are shown in Fig. 3. The computational volume and the numerical mesh are created using the software package GAMBIT.[13] The most convenient Cooper scheme[14,15] is not valid for the showerhead geometry of two nonparallel cylindrical volumes; therefore, the reactor geometry is decomposed into two subdomains (showerhead and cone/cylinder working space) to apply the Cooper tool for grid generation in each subdomain.

To mesh the cone/cylinder working space, the near-wall structural grid clustering, denoted as a grid boundary layer, is applied first. The grid cell hight closest to the wall is equal to $0.25r_0 (\approx 0.0118R)$, the number of boundary-layer grid nodes is 10, and the growing coefficient of the grid size is 1.02 (Fig. 3). The rest of this subdomain is covered with hexahedral elements with $1r_0$ size using the Cooper algorithm. The axial section of the grid and the exit cross section are shown in Fig. 3.

The showerhead (Fig. 4) is meshed by the Tet/Hybrid option of GAMBIT ($0.25r_0$ grid size) which composes the mesh primarily of tetrahedral mesh elements, but may include hexahedral, pyramidal, and wedge elements where appropriate. The total number of numerical grid cells is 372,993. Because the reactor is periodic with angular span 120 deg, at attempt was to compute only one-third of the geometry with symmetry conditions applied on the cutting planes. However, the symmetry boundary conditions deteriorate the convergence rate, and this approach was not pursued further.

B. Mathematical Model and Solution Algorithm

To model the flowfield, the three-dimensional, Reynolds-averaged Navier–Stokes (RANS) equations are combined with a renormalization group (RNG) k–ϵ turbulence model.[16,17] Gas density and compressibility are described by the ideal gas model. Because jets intersect within 3–4 diameters from their exits, their centerline velocity is equal to the jets' initial velocity. Note that, at such a distance from the jet nozzle, the cross-sectional velocity profile is neither uniform nor self-similar.[18] The momentum flux ratio, $(\rho u^2)_c/(\rho u^2)_p$, where indices c and p denote central and peripheral jets, respectively, is equal to 1.39, that is, close to unity. Also, the cross sections of the jets are of the same order of magnitude, and none of the jets can be approximated by a uniform and infinitely wide crossflow.

According to Sutherland's law, the viscosity is given by

$$\mu = \frac{C_1 T^{\frac{3}{2}}}{T + C_2} \tag{1}$$

where for carbon oxide $C_1 = 1.657 \times 10^{-5}$ and $C_2 = 273.11$. The calculated viscosity is $\approx 20 \times 10^{-5}$ kg/(m × s) for 100°C and $\approx 50 \times 10^{-5}$ kg/(m × s) for 1050°C. Viscosity of two-atom gases is almost constant with pressure up to 40 atm (see Ref. 19, pp. F12–F15). Recall that the cold jet has a temperature of 373 K and a flow velocity of 37 m/s. For the central cold jet, the Reynolds number is given by

$$Re = \frac{37 \text{ m/s} \times 10^{-3} \text{ m} \times 1.12 \text{ kg/m}^3 \times 30 \text{ atm} \times 373/273}{20 \times 10^{-5} \text{ kg/(m} \times \text{s)}} \approx 8500 \tag{2}$$

For peripheral hot jets,

$$Re = \frac{59 \text{ m/s} \times 1.5 \times 10^{-3} \text{ m} \times 1.12 \text{ kg/m}^3 \times 30 \text{ atm} \times 1323/273}{50 \times 10^{-5} \text{ kg/(m} \times \text{s)}} \approx 29{,}000 \tag{3}$$

Nevertheless, the RNG k–ϵ model of turbulence is used in this study because it takes into account the low-Reynolds-number effects in the downstream cylindrical part of the reactor and in the near-wall recirculation zones.

The governing equations are three-dimensional steady RANS equations. Boundary conditions for inlet jets are taken as uniform velocity profiles taken at distance $7r_0$ upstream of the central nozzle exit and at distance $3r_p$ upstream of the peripheral nozzle exit. The turbulence intensity, that is, the ratio of the root-mean-square of the velocity fluctuations to the mean flow velocity, is taken equal to 10%. Recall that the inflow turbulence intensity is high because the jets have been passed through a compressor. The one-dimensional outflow boundary conditions are specified with a static (gauge) pressure at the outlet set equal to zero. Because the walls of reactor are preheated to keep peripheral jets at high temperature (Fig. 1), isothermal boundary conditions are adopted with 1373-K wall temperature.

Standard wall functions proposed in Ref. 20 are used. The nondimensional distance from point P to the wall is given by

$$y^* = C_\mu^{0.25} k_P^{\frac{1}{2}} y_P \big/ \nu \tag{4}$$

where $C_\mu = 0.09$, k_P is turbulent kinetic energy at point P, y_P is the distance from near-wall numerical grid point to the wall, and ν is the kinematic molecular viscosity of the gas. The transport equation for turbulent kinetic energy is solved in the whole domain including the near-wall points P. The boundary condition $\partial k/\partial n = 0$, where n is the local coordinate, is imposed at the wall. The dissipation rate of kinetic energy is computed on the basis of the local equilibrium hypothesis, that is, the production of k and its dissipation rate are assumed to be equal in the wall-adjacent control volume. The ϵ is computed from

$$\epsilon^P = \frac{C_\mu^{\frac{3}{4}} k_P^{\frac{3}{2}}}{k y_P} \tag{5}$$

The transport equation for ϵ is solved using the computed value ϵ_P as a boundary condition. The values of y^* computed in the numerical grid used exceed 50 at the reactor walls. Therefore, the near-wall numerical grid point P is located beyond the buffer layer, and the dimensionless velocity assumes a logarithmic profile as a function of the dimensionless distance from the wall y^*.

The solution algorithm solves the governing equations sequentially, that is, it exploits the low Mach number formulation. The working pressure of the reactor is 30 atm. In the frame of ideal gas approach, the speed of sound and the flow Mach number remain the same as they were for standard atmospheric pressure, that is, the jets' Mach numbers are below 0.1. At each iteration, the density is recomputed using the ideal gas law. Because the temperature variations are large, the additional density dependence on pressure does not affect the convergence speed.

The directional momentum equations are each solved in turn using current values for pressure and cell face mass fluxes, to update the velocity field. Because the velocities obtained may not satisfy the continuity equation locally, a Poisson-type equation for the pressure correction is derived from the continuity equation and the linearized momentum equations (see Ref. 21). This pressure correction equation is then solved to obtain the necessary corrections to the pressure and velocity fields and the face mass fluxes such that continuity is satisfied. Equations for scalars such as turbulence and radiation are solved using the previously updated values of the other variables.

Second-order accuracy spatial discretization is used for the viscous terms. FLUENT permits a choice of discretization scheme for the convection terms of each governing equation. For tetrahedral grids, because the flow is never aligned with the grid, the first-order convective discretization increases the numerical diffusion, and more accurate results can be obtained by using the second-order upwind discretization of convective terms.[22] However, the first-order discretization generally yields better convergence than the second-order scheme; therefore, in the current study computations start with the first-order scheme for all equations and then

switch to the second-order scheme (also for all equations) after some iterations.

FLUENT provides three methods for pressure–velocity coupling (discussed earlier) in the segregated solver: SIMPLE, SIMPLEC, and PISO. The pressure-implicit with splitting of operators (PISO)[23] pressure–velocity coupling scheme, part of the SIMPLE family of algorithms,[21] is based on the higher degree of the approximate relation between the corrections for pressure and velocity. PISO with skewness correction is recommended for calculations on meshes with a high degree of distortion.

The algebraic multigrid (AMG) is used to solve linearized systems at each time step (iteration). This algorithm is referred to as an algebraic multigrid scheme because the coarse level equations are generated without the use of any geometry or rediscretization on the coarse levels, a feature that makes AMG particularly attractive for use on unstructured meshes.

After discretization, the conservation equation for a variable ϕ at a cell P is written as[21]

$$a_P \phi_P = \sum_{nb} a_{nb} \phi_{nb} + b \tag{6}$$

The residual is the imbalance in Eq. (6) summed over all computational cells:

$$R_\phi = \sum_{\text{allcells}} \left| a_P \phi_P - \left(\sum_{nb} a_{nb} \phi_{nb} + b \right) \right| \tag{7}$$

The scaled residual is defined as

$$R_\phi = \frac{\sum_{\text{allcells}} \left| a_P \phi_P - \left(\sum_{nb} a_{nb} \phi_{nb} + b \right) \right|}{\sum_{\text{allcells}} |a_P \phi_P|} \tag{8}$$

In momentum equations, ϕ_P is replaced by V_p, where V_P is the magnitude of the velocity at cell P. Therefore, the scaling factor for a variable ϕ is a representative of the flow rate of ϕ through the domain. The used convergence criterion requires that the scaled residuals [Eq. (8)] decrease to 10^{-3} for all equations.

The convergence in terms of the scaled residuals $R(\phi)$ as the function of the number of iteration for continuity (curve 1), velocities in the x and y directions (coinciding curves 2 and 3), velocity in the axial direction z (curve 4), turbulent energy k (curve 5), and the dissipation of turbulent energy ϵ (curve 6) are presented in Fig. 5. The spike in the convergence curves at iteration 26 corresponds to the switch from the first-order approximation of convective terms to the second-order approximation with the PISO pressure–velocity coupling algorithm before the iterations are completed. Because

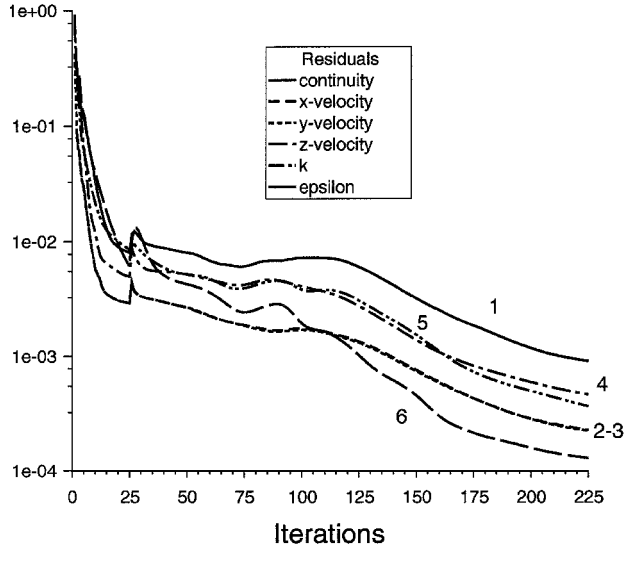

Fig. 5 Convergence history: 1) continuity, 2) and 3) x and y velocities, 4) velocity in the axial direction z, 5) turbulent energy k, and 6) dissipation of turbulent energy.

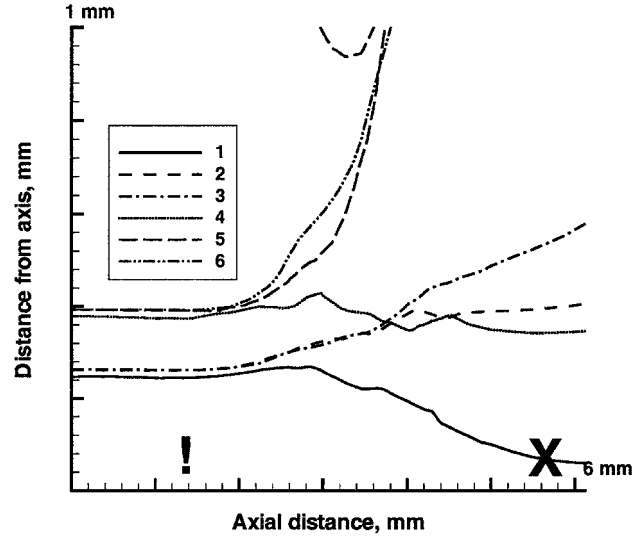

Fig. 6 Grid refinement studies: trajectories of catalyst particles on refined grid for case A30-D.

initial values of all variables are set equal to zero everywhere except at the inlet, the initial values of residuals [Eq. (8)] are close to unity.

In addition to solving transport equations for the continuous phase in the Eulerian framework, FLUENT has an option to simulate a discrete second phase in a Lagrangian frame of reference that includes the hydrodynamic drag and the discrete phase inertia. In our case, the inertia is negligible because the catalyst particles are of micrometer size; therefore, the particle trajectories coincide with the flow pathlines, that is, the streamlines of the steady RANS model. Also, the particles temperature is equal to the local gas temperature. The influence of turbulent dispersion will be discussed in Sec. V.

To check the sensibility to grid refinement, the numerical grid size is halved: The showerhead is meshed with $0.125r_0$ grid size, and the cone/cylinder working space is covered with $0.5r_0$ grid size. The six representative pathlines for case A30-D are presented in Fig. 6. The trajectories of catalyst particles appear to be close to those for the regular mesh size (compare Figs. 6 and Fig. 7b).

IV. Single Central Jet: Results and Discussion

First, computations were performed for a single central jet and three peripheral jets in the reactor described in Sec. II and denoted as design A. The angle between the central and a peripheral jets is taken equal to 30, 60, and 90 deg, whereas the mass ratio M is taken equal to 1:3 and 1:6. (In the latter case the peripheral jet velocity is doubled.) The cases are denoted as A30, A30-D, A60, A60-D, A90, and A90-D where the number after the letter A is the angle between the central and peripheral jets and the letter D means doubled hot-gas consumption. For special cases of design A, where $\alpha = 90$ deg, nozzles are located farther downstream at the reactor funnel, $z = 3.1$ mm, to avoid interaction between peripheral jets and the internal cylinder surrounding the central jet nozzle.

Design B of the reactor has a cylindrical workspace with the radius of cross section equal to the entrance radius R_1 of the conical part of design A. Design B has two opposite peripheral jets with the same exit radius r_p as for design A.

The computed flowfield is presented in Figs. 8a and 8b for two limiting cases: $\alpha = 30$ deg, $M = 1{:}3$, and $\alpha = 90$ deg, $M = 1{:}6$ for designs A30 and A90-D, respectively.

The velocity vectors are colored by the local flowfield temperature. The vectors are presented in the x–z plane ($y = 0$). The centerline of the peripheral jet is located in this plane, and so the interaction between the central and the peripheral jet in the plane of their centerlines is clearly seen in the left side of Figs. 8a and 8b. The right-hand side of the plane in Figs. 8a and 8b is located between two other peripheral jets. In case A30, the peripheral jet merges with the central jet without the formation of a significant recirculation zone upstream of the intersection. On the contrary, the strong recirculation zone

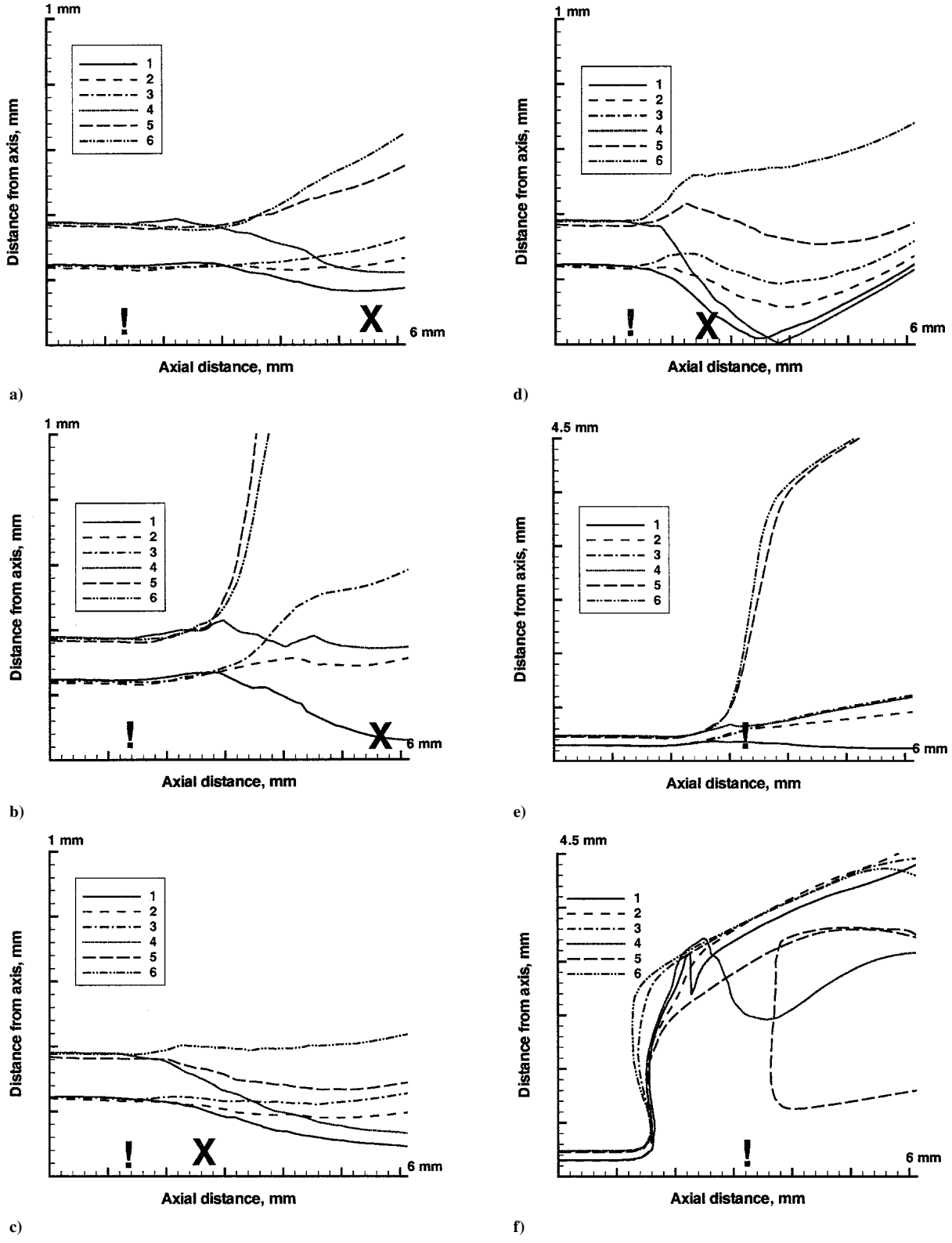

Fig. 7 Trajectories of catalyst particles; x, geometric point of the jets' intersection at the reactor centerline and !, cross section with peripheral nozzles: a) A30, b) A30-D, c) A60, d) A60-D, e) A90, and f) A90-D.

between the central and the peripheral jet is formed in case A90-D. Vortices are located aside of the jet centerlines and the low-speed stagnation zone appears upstream of the intersection of the jets near the central jet centerline. For case A90-D, the momentum flux ratio between the central and a peripheral jet is equal to 0.35, the peripheral jet reaches the intersection point without the formation of stagnation zone at its centerline.

The material of the central jet spreads aside between the peripheral jets. In case A30 (Fig. 8a), most of the flow vectors in the spreading region are directed in the z direction, whereas in the case A90-D, the flow vectors are directed backward and form the recirculation zone near the reactor side wall.

The observed difference in jet interaction between cases A30 and A90-D is caused by the fact that in the latter case the velocity component $|u|$ (normal to the central jet) is four times [$2/\sin(30\ \text{deg}) = 4$] larger than that in the former case.

Compare our results with the study[2] where the uniform cross-flow interacts with the row of jets issuing perpendicular to the crossflow.

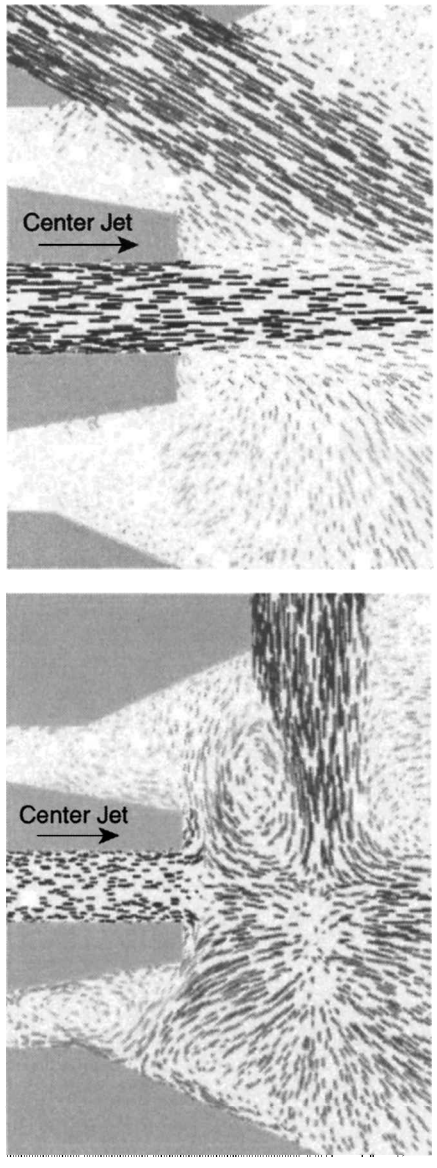

Fig. 8 Flowfield in the x–z section: a) A30 ($\alpha = 30$ deg, $M = 1{:}3$) and b) A90-D ($\alpha = 90$ deg, $M = 1{:}6$).

The authors of Ref. 2 observed the formation of vortices downstream and upstream of the jet row, which they call primary and secondary vortices, respectively. In our case, the upstream vortex is larger and stronger than the downstream vortex because of the cross-sectional non-uniformity of the central jet (as opposed to the uniform crossflow). The peripheral part of the central jet has relatively low velocity and easily forms the vortex upstream of the peripheral jet, which can be viewed as a rigid obstacle. Also, the upstream vortex affects the heating rate more along the central jet path lines than the downstream vortex.

If the jet is strong enough, the crossflow forms vortices around the jet rather than penetrating it. When the jet strength weakens far downstream from its exit, the crossflow is able to penetrate the jet and eventually split it.[2] In our case, the cross-sectional nonuniformity of the central jet and weakening of the peripheral jets (due to their counterflow type of interaction with each other) leads to a situation where the peripheral part of the central jet forms a vortex, whereas the central part of this jet penetrates the peripheral jet. Both phenomena occur within approximately the same distance from the exit of the peripheral jet. This determines different mixing scenarios for various catalyst particles issuing uniformly from the central jet nozzle.

To study the temporal temperature profile, six pathlines were chosen to represent catalyst particle trajectories (Fig. 9) The initial radial

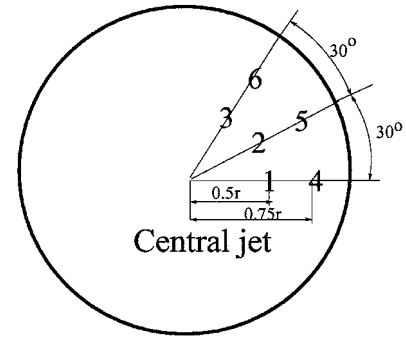

Fig. 9 Issuing points of the six pathlines for design A.

distance from the center of the central nozzle is equal to $0.5r_0$ for the first three (inner) trajectories and $0.75r_0$ for the remaining (outer) trajectories. The angular coordinates in the nozzle cross section x–y are $\beta = 0$, 30, and 60 deg. The first angular location is in the peripheral jet plane x–z, whereas the last location is exactly between two peripheral jets. Recall that the reactor is periodic in the cross section with the angular span 120 deg.

The temperatures along the trajectories as a function of time for cases A30, A30-D, A60, A60-D, A90, and A90-D are shown in Figs. 10a–10f, respectively.

To get more insight into how the particles are heated, the distance from the reactor axis along particle trajectories $\sqrt{(x^2 + y^2)}$ as a function of the axial coordinate z is plotted in Figs. 7a–7f. The cases and the pathlines are the same as in Fig. 10. In Fig. 7, the cross-section corresponding to the peripheral nozzles and geometric intersection of the jets' axes are shown at the horizontal axis, symbols ! and x, respectively.

For $\alpha = 30$ deg, the trajectories that are directly exposed to the core of the peripheral jet ($\beta = 0$) are inclined toward the centerline, that is, they belong to the first category of trajectories (Fig. 2). The remaining pathlines are inclined outward, that is, they fall into the second category of trajectories (Fig. 2). The outer trajectories are bent higher and heated faster than the inner trajectories. The degree of bending primarily depends on the speed of the peripheral jets. (Compare the corresponding trajectories in Fig. 7a and Fig. 7b.) The heating rate along the trajectories of the first type is the slowest, whereas the heating rate along the remaining trajectories increases with the initial radius and the initial angular position β.

Increasing the angle between jets up to $\alpha = 60$ deg leads to the bending of the trajectories considered toward the centerline (Figs. 7c and 7d). In spite of the reduced spatial scale of the mixing zone, the temporal scale increases, that is, the heating rate drops in comparison with the earlier case. The only trajectory that is substantially bending outward, has an initial position between the peripheral jets (Fig. 10d, curve 6) and this trajectory has the best heating among all trajectories in case A60-D (Fig. 10d, curve 6). Other trajectories in cases A60 and A60-D have nonmonotonic behavior of their radial coordinate as a function of axial coordinate. Behavior of the latter trajectories leads to the worst performance in terms of the heating rate of all considered angles α for design A (Fig. 11).

Further increase of the angle between jets up to $\alpha = 90$ deg changes the behavior of the trajectories so that those with initial positions between the peripheral jets are highly bent outward (Fig. 7e, curves 5 and 6). For $M = 1{:}6$, some trajectories show closed loops, that is, they fall into the third category. For case A90, the angle between jets provides higher heating rate; however, strong temperature oscillations are observed (Fig. 10e). For case A90-D, trajectories show nonmonotonic behavior of axial coordinate, which leads to closed loops for some of trajectories (Fig. 7f). In this case, the most of particles are not heated up to 1100 K because they are involved in recirculation upstream of the jet intersection point.

Increasing the mass ratio up to $M = 1{:}12$ (Figs. 12a and 12b) bends some trajectories inward, whereas the rest of particles are involved in the rotating motion (Fig. 12b compared with Figs. 7e and 7f). The temperature profiles along the trajectories show large oscillations.

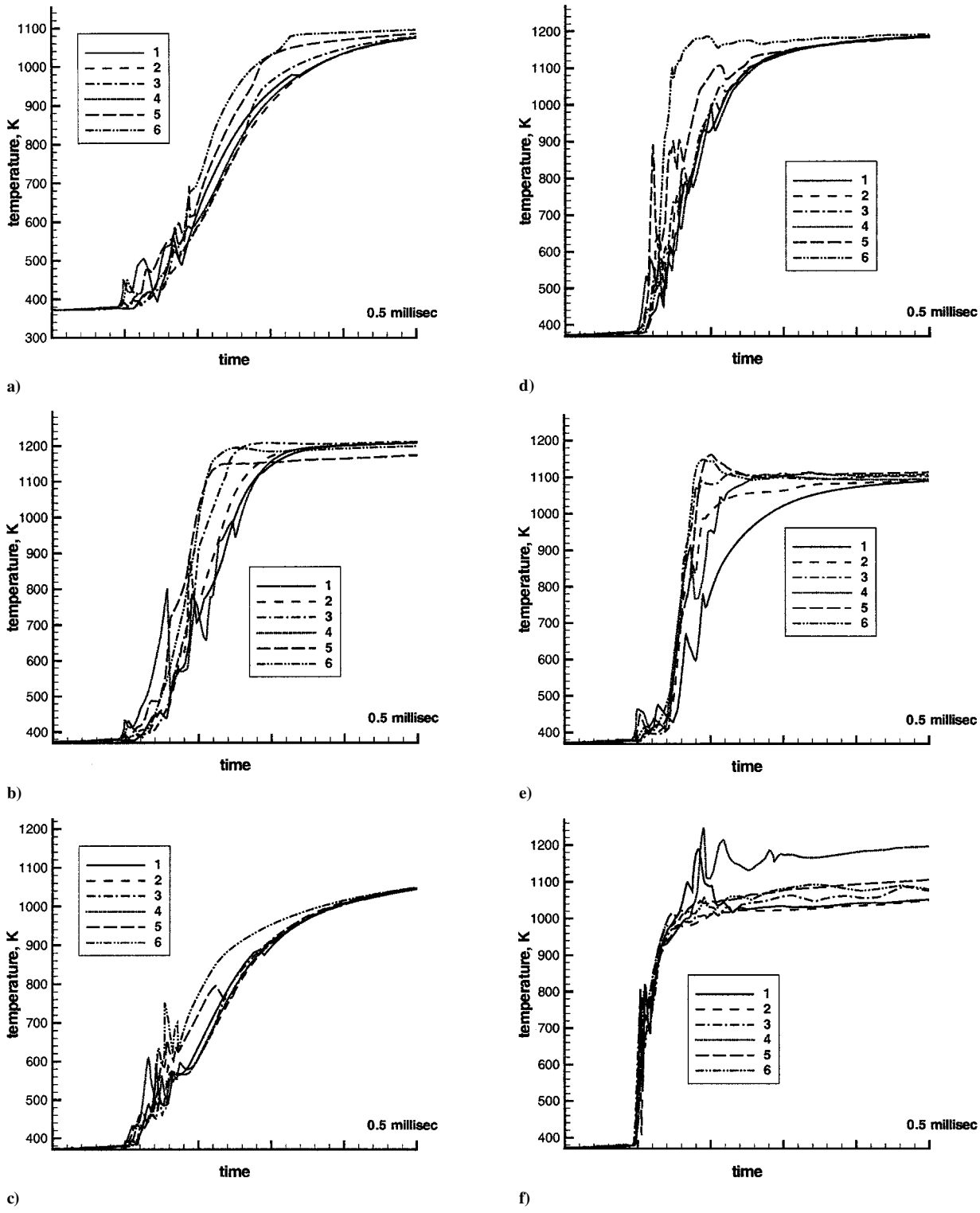

Fig. 10 Temperatures of catalyst particles: a) A30, b) A30-D, c) A60, d) A60-D, e) A90, and f) A90-D.

Design B, which has 90-deg angle of jet intersection, $M = 1{:}6$, and two strong peripheral jets, shows the worst scenario of particle heating. The slow heating along trajectories together with large temperature oscillations is caused by the rotational nature of the trajectories (Figs. 12c and 12d).

The heating rate dT/dt (degrees Kelvin per second) at 800 K as a function of the angle between jets for design A is presented in Fig. 11b. The angle between the central and peripheral jets is taken as 30, 45, 60, 75, and 90 deg. Temperature profiles and coordinates of trajectories are presented in Figs. 7 and 10 for 30, 60, and 90 deg. The local minimum at 60 deg corresponds to the case where trajectories belong to the first category (Figs. 7b and 10b). At $\alpha = 45$ deg, the trajectories are qualitatively similar to those at 30 deg (Fig. 7a); however, they are more bent outward, and the heating rate reaches a local maximum. For the angles higher than 60 deg, the heating rate strongly increases; however, the temperature profiles are oscillatory. For instance, two of six temperature curves cross the line 800 K more than once at 75 deg, and four curves do so at 90 deg. The heating rate becomes a multivalued function of temperature for some trajectories; only the maximum value of heating rate is presented in Fig. 11.

To summarize, the goal of increasing the heating rate while avoiding temperature oscillations cannot be achieved by straightforward measures such as, increasing hot-gas consumption or increasing the

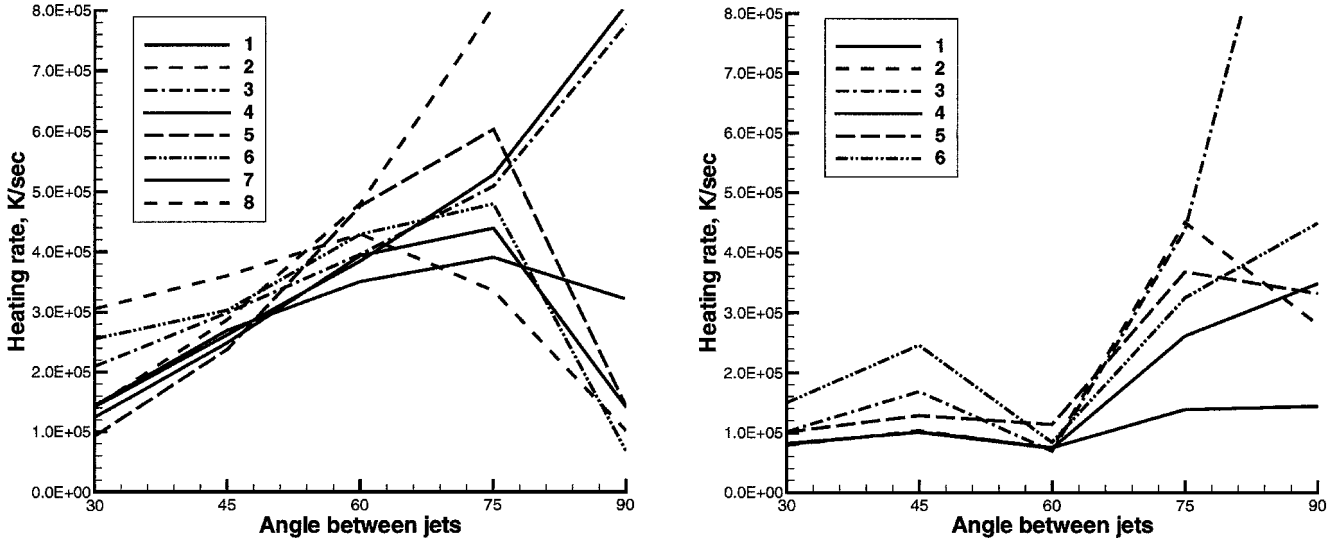

Fig. 11 Heat rate at 800 K as a function of angle between jets: a) design C and b) design A.

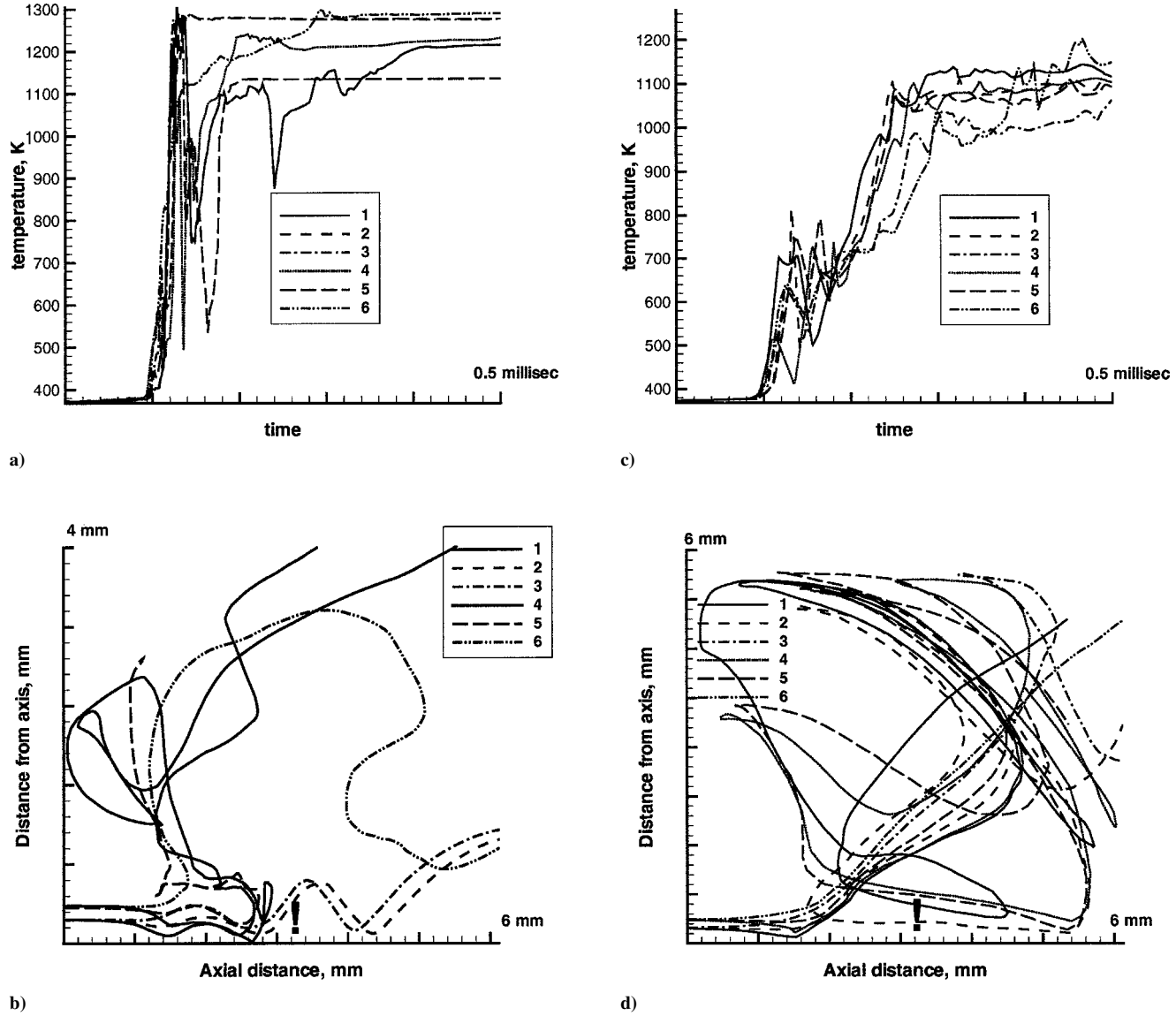

Fig. 12 Temperatures and trajectories of catalyst particles for enhanced peripheral jet velocity: a) and b) mass ratio: 1:12 and c) and d) reactor B, two peripheral jets, mass ratio 1:6.

angle between hot and cold incident jets. The reason for this is the behavior of path lines. Inward-bending pathlines (category 1) show slow heating, whereas rotating pathlines (category 3) have highly oscillating temperature profiles. Although the high angle between mixing jets leads to very short-scale spatial mixing, the heating of catalyst particles is relatively slow, and the temperature oscillates along the particle trajectories.

V. Reactor with Three Central Jets

To increase the heating rate along trajectories, a modified reactor design was proposed that includes three parallel nozzles for cold central jets. Two variants of this design are design C and design D (described subsequently).

The radius of the central nozzles is chosen to keep the same overall cross-sectional surface as that for the single central nozzle, that is, $r_c = r_o/\sqrt{(3)}$. The centers of the central nozzles are located at a distance $2r_c$ from the reactor centerline and form an equilateral triangle. The peripheral jets are arranged as in the basic design A.

In design C, a plane containing the reactor centerline and a central jet nozzle makes an angle of 60 deg with the peripheral jet nozzle planes (Fig. 13a). In design D, central jet nozzles and corresponding peripheral jet nozzles are in the same plane.

Design D represents a straightforward split of the single central jet into three straight central jets and is examined first. The three jets are equivalent; therefore, the six trajectories are chosen to issue from the same jet. As in the earlier cases, initial radial distance from the center of the central nozzle is taken equal to $0.5r_c$ for the

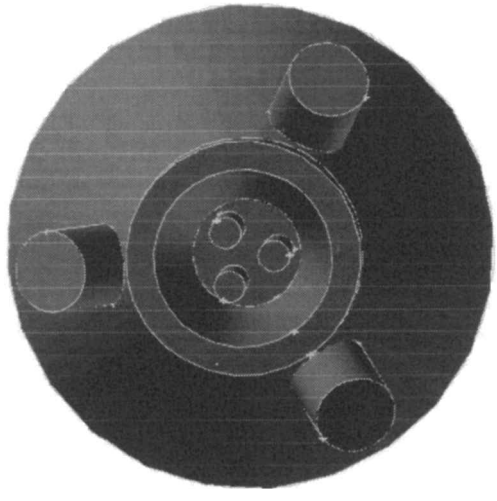

a)

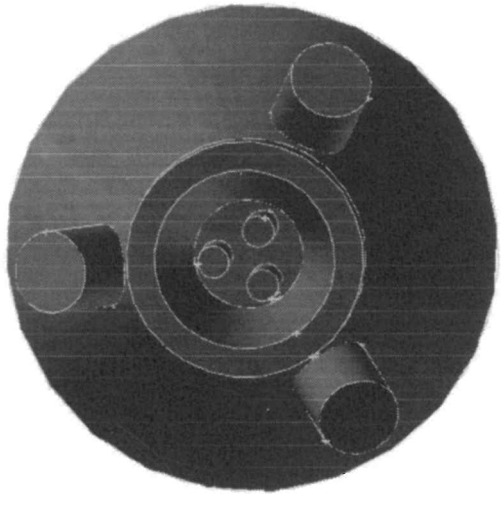

b)

Fig. 13 Showerheads: a) design C and b) design D.

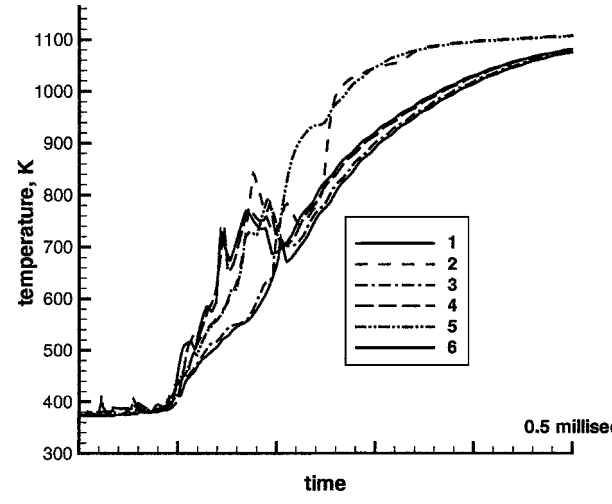

a)

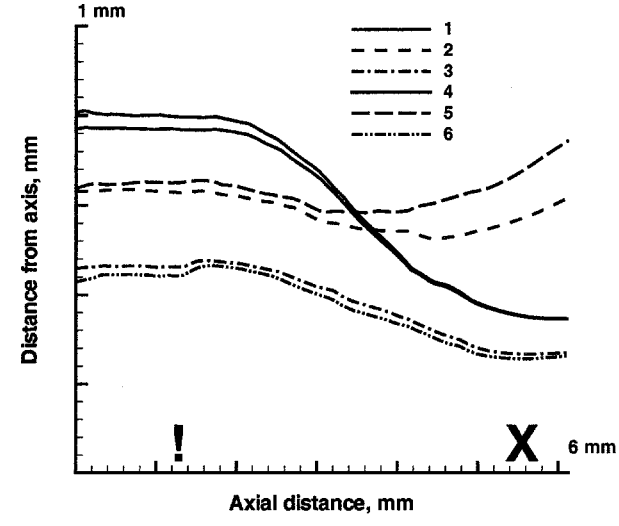

b)

Fig. 14 Temperature and trajectories of catalyst particles for case D3, $\alpha = 30$ deg.

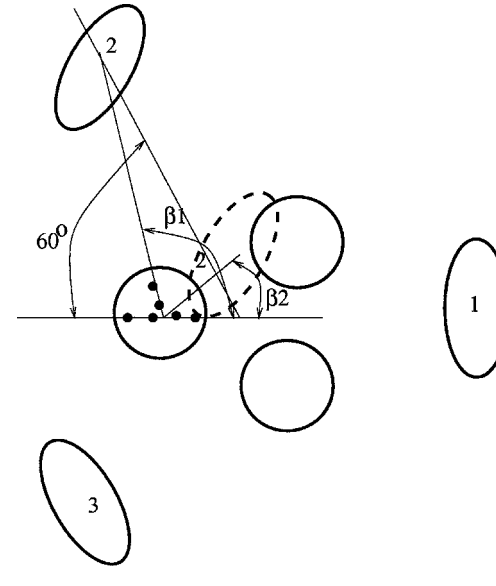

Fig. 15 Issuing points of considered pathlines for design C: dashed ellipse, approximate final cross section of the peripheral jet and •, initial positions of the considered pathlines.

first three trajectories and $0.75r_c$ for the remaining trajectories. The angular coordinates are taken as $\beta = 0, 90, 180$, and 270 deg. Results for $\alpha = 30$ deg are presented in Figs. 14a and 14b. Unfortunately, the heating rate is worse than for the single central jet. (Compare Fig. 14a with Fig. 10a.)

The reason for the slow heating is that all trajectories are bent toward the reactor centerline (Fig. 14b). Therefore, the straightforward split of the central jet does not help to achieve high heating rate.

To avoid direct exposure of the trajectories to the action of the hot jets, design C is based on a rotation of the location of central and peripheral nozzles (Figs. 13a and 15). To show the most critical trajectories, the initial and final cross sections of peripheral jets and central jets are presented in Fig. 15. The initial positions of the three peripheral jets (projection on a cross section x–y) are shown as ellipses and denoted 1, 2, and 3. The final position of one of the peripheral jets is shown as a dashed ellipse. The two initial angular positions of trajectories are chosen as $\beta = 0$ and 180 deg. The former location is the closest to jet, 1 whereas the latter location is the most peripheral. The choice of the initial location of the remaining couple of trajectories (closest to the jets 2 and 3) is not straightforward; the mutual location of central and peripheral jets in x–y cross sections is varied with the axial coordinate z. Angle

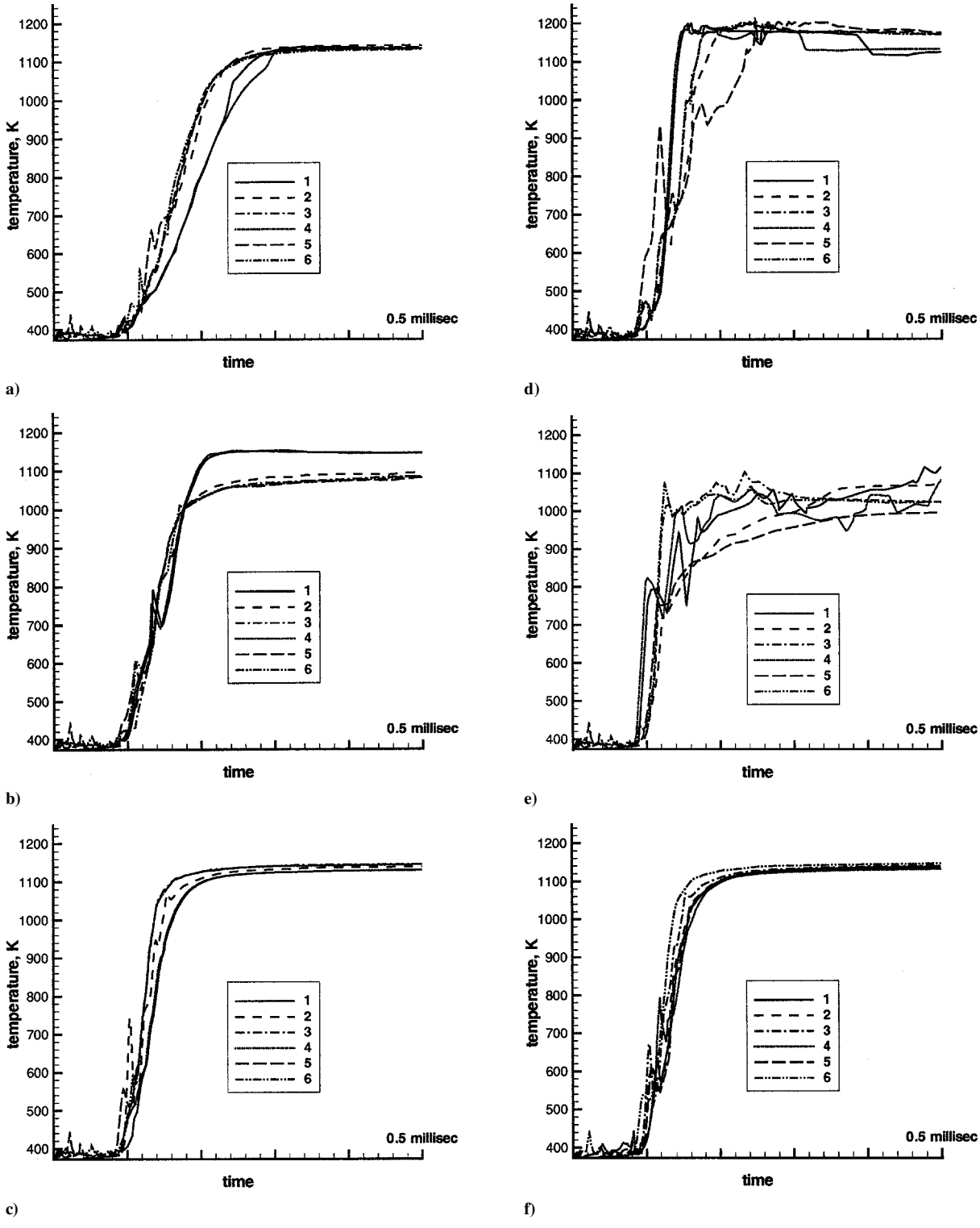

Fig. 16 Temperatures of catalyst particles for three central parallel jets; angle α between the reactor axis and peripheral jets: a) $\alpha = 30$ deg, b) $\alpha = 45$ deg, c) $\alpha = 60$ deg, d) $\alpha = 75$ deg, e) $\alpha = 90$ deg, and f) $\alpha = 60$ deg, $\beta = \beta_1$, β_2, and β_{av}.

β_1 corresponds to the exit of peripheral jet 2, whereas the angle β_2 corresponds to the approximate final location of the peripheral jet 2 before it merges with other peripheral jets. Angles β_1 and β_2 are calculated from corresponding triangles. Angle $\beta_{av} = 0.5(\beta_1 + \beta_2)$ is taken as an averaged angle between two limit positions. For the given reactor geometry, $\beta_1 = 108.1$, $\beta_2 = 72.9$, and $\beta_{av} = 90.5$ deg. The temperature profiles along trajectories with angular locations β_1, β_2, and β_{av} are similar to each other (Fig. 16f; $\alpha = 60$ deg).

In Figs. 16–18, the angle β_1 is chosen for the representative trajectory. For $\alpha \leq 60$ deg (Figs. 17a and 17b) the trajectories fall into

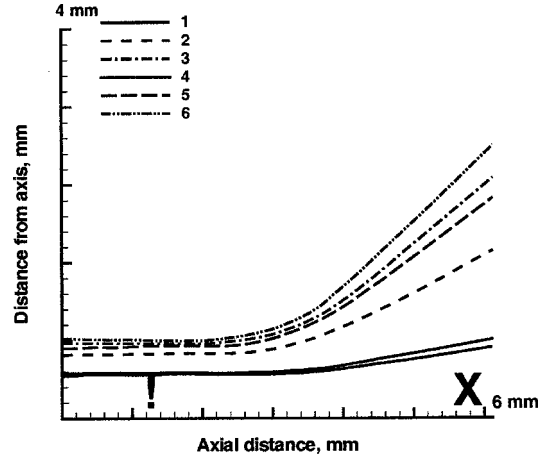

a)

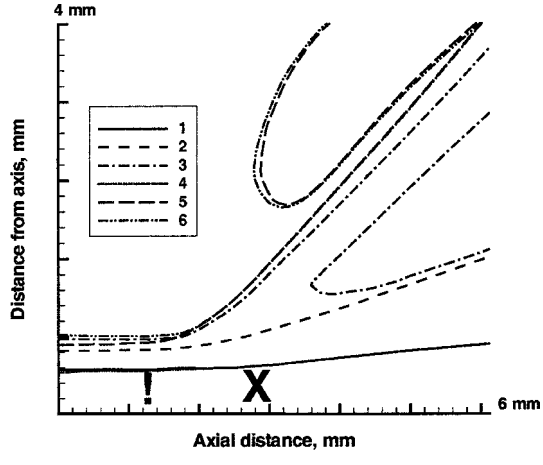

b)

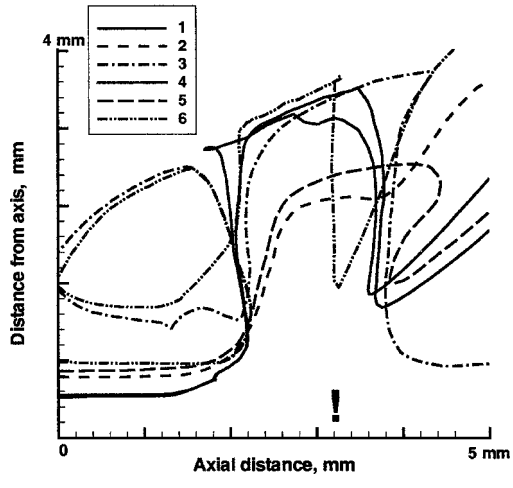

c)

Fig. 17 Trajectories of catalyst particles for three central parallel jets; angle α between the reactor axis and peripheral jets: a) $\alpha = 30$ deg, b) $\alpha = 60$ deg, and c) $\alpha = 90$ deg.

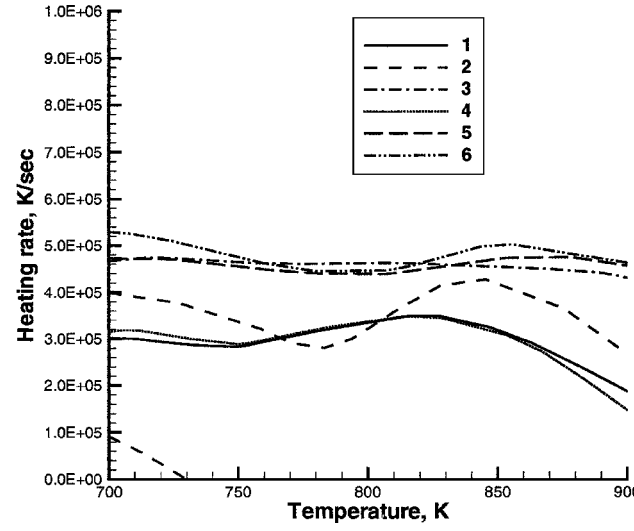

Fig. 18 Heat rate of catalyst particles vs temperature for $\alpha = 60$ deg. Temperature interval 700–900 K taken.

the second category. The most bent trajectories have initial position $\beta = 180$ deg, whereas trajectories with initial $\beta = 0$ deg remain least bent. As opposed to design A, no first-type trajectories are observed. (Compare Figs. 17a and 17b with Figs. 7a and 7c, respectively.) This is the major advantage of design C, leading to considerably higher heating rate than that for design A. (Compare Figs. 16a–16c and 16f with Figs. 10a and 10c.) For design C, the optimal nozzle arrangement with $\alpha = 60$ deg provides a heating rate $3.5–4.8 \times 10^5$ K/s, where $T = 800$ K (Fig. 18). On the contrary, for design A with its optimal $\alpha = 45$ deg, the heating rate is in the range $1–1.5 \times 10^5$ K/s.

Although further increase of the angle between jets to 75 deg provides higher heating rate than that for 60 deg (Fig. 11a), some trajectories appear to switch to the third type. For 90-deg angle between jets, the trajectories become highly rotating (Fig. 17c), and temperature profiles strongly oscillate (Fig. 16e).

For design C ($\alpha = 60$ deg), the flowfield in the longitudinal section (x–z plane) is presented in Fig. 19a. The velocity vectors of a cold central jet are directed outward, and no significant longitudinal vortices are observed. In fact, the visible peripheral jet, which corresponds to the jet 1 in Fig. 15, interacts with the visible central jet after the peripheral jets merge, resulting in annihilation of their normal velocity components. In the cross section with the z coordinate corresponding to the jets' intersection point (Fig. 19b), the material of the central jets is directed outward between the peripheral jets. The vortices appear due to interaction of these outward-directed fluxes with the reactor wall. However, the particles have already been heated before they enter these vortices.

Particle trajectories considered earlier coincide with streamlines of the RANS steady flow computed by the Eulerian approach. However, for turbulent jet mixing particle trajectories deviate from streamlines of the steady flow and the validity of the RANS-based approach to trajectory-based optimization of reactor will be discussed here.

Because the flow is turbulent, the molecular (laminar) diffusion induced by Brownian motion is small in comparison to turbulent diffusion. The thermophoresis is a phenomenon where small particles suspended in a gas that has a temperature gradient experience a force in the direction opposite to that of the gradient. This phenomenon is explained by the presence of viscous force with temperature-dependent molecular viscosity. For turbulent motion, the thermophoresis effect is usually small because the molecular viscosity is small in comparison with the turbulent viscosity. We added the thermophoretic force (in the form suggested by Talbot et al.[24]) in the particle dynamic equation; however, this addition does not affect the trajectories of particles in the considered turbulent flow.

The turbulent dispersion of particles is predicted by integrating the dynamic equation for individual particles using the instantantaneous fluid velocity $U = \bar{U} + U'$ along the particle path during the

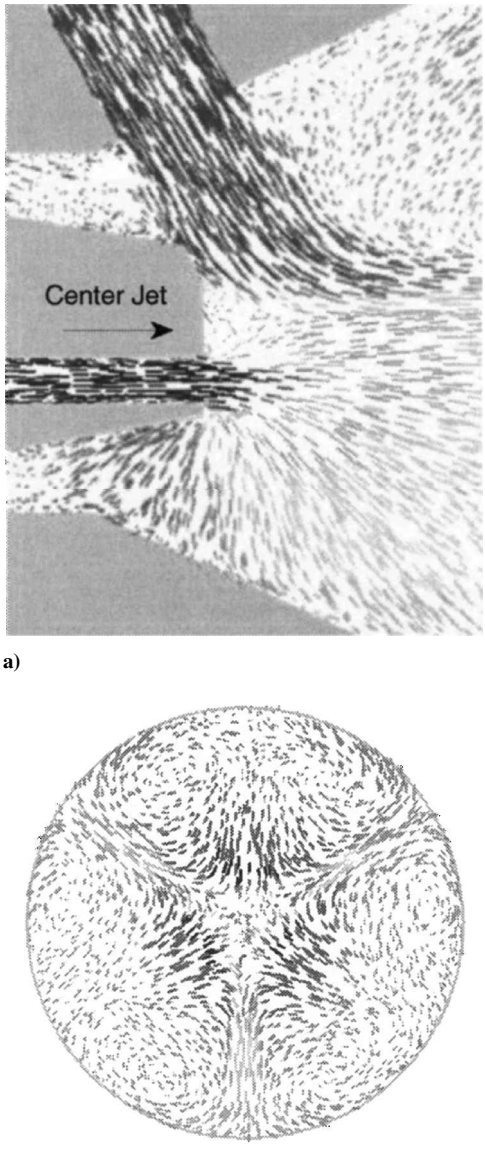

a)

b)

Fig. 19 Flowfield, design D, $\alpha = 60$ deg: a) x–z plane, velocity vectors shaded by the local temperature and b) x–y cross-section at jet intersection point.

integration. In FLUENT, the discrete random walk (DRW) model is used. In this model, the fluctuation velocity components are discrete piecewise constant functions of time. Their random value is kept constant over an interval of time given by the characteristic lifetime of the eddies. The fluid Lagrangian integral time is approximated as

$$t_L = C_L(k/\epsilon) \tag{9}$$

where the constant $C_L = 0.15$ (Ref. 11).

In Fig. 20, the pathlines of particles which are computed using the DRW are presented for design A, case A60-D, and for design C, $\alpha = 60$ and $\alpha = 90$ deg. By comparison with averaged pathlines for corresponding cases (Figs. 7d and 17b and 17c), the qualitative similarity could be observed. For case A60-D, five trajectories are bent inward (type 1) and one trajectory is bent outward (type 2). For design C ($\alpha = 60$ deg), trajectories are bent outward and two of them are involved in rotational motion downstream. For design C ($\alpha = 90$ deg), all trajectories are of type 3 and involved in recirculation upstream of the interception point.

Evidently, the trajectories computed by DRW model do not coincide with streamlines of the RANS flow. In the current computations, the distance between the initial cross section and the nozzle

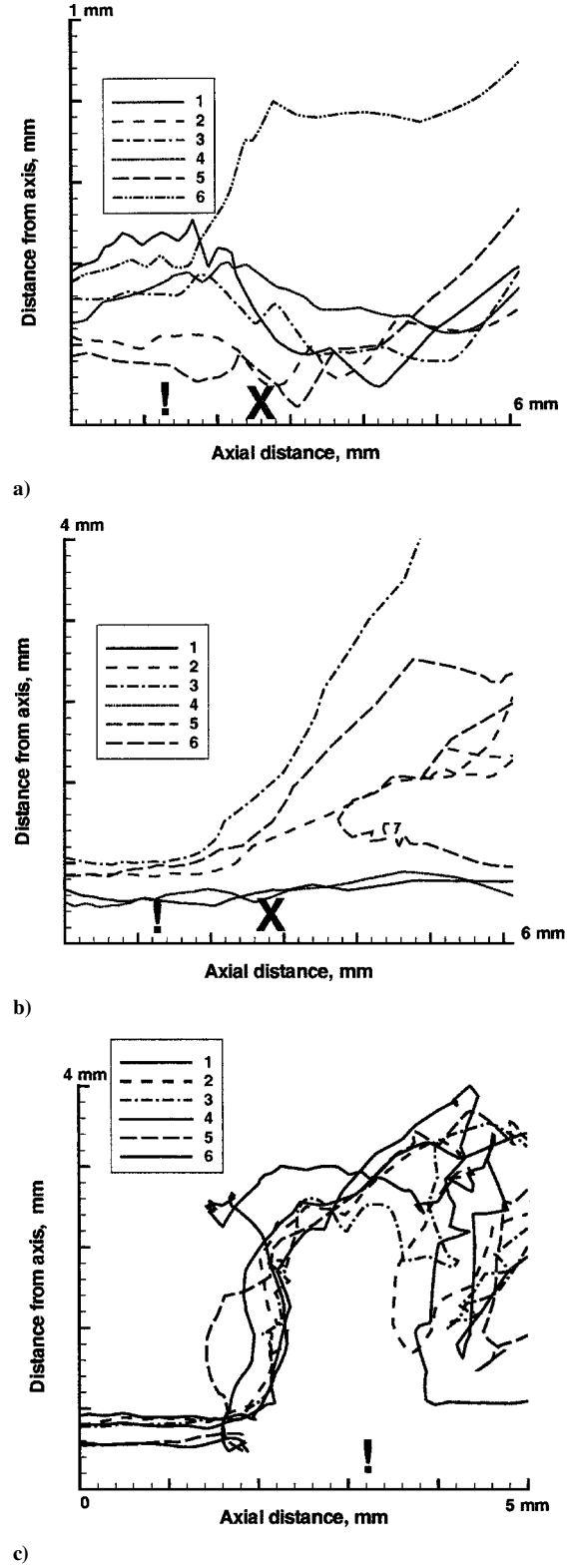

Fig. 20 Trajectories of catalyst particles with DRW model for turbulent dispersion: a) design A, case A60-D; b) design C, $\alpha = 60$ deg; and c) design C, $\alpha = 90$ deg.

orifice is moderate, $7r_0$. Yet, the deviation of pathlines from averaged streamlines is visible (leftmost coordinates of pathlines in Figs. 7, 17, and 20). If the issuing cross section is taken farther upstream of the nozzle orifice, the coordinates (x, y) of pathlines at the nozzle orifice may be completely different from their original values (according to well-known Reynolds experiments), and therefore, the steady streamlines no longer follow pathlines of individual particles in the turbulent flow. Nevertheless, the representative set

of steady streamlines shows how many trajectories of the total set obey various types of pathlines behavior analyzed in this paper. This evaluates the mass fraction of well-heated particles for a particular setup of nozzles, and therefore, the steady trajectories could be used for the purpose of reactor optimization.

VI. Conclusions

Mixing of cold and hot jets in a reactor with a high angle between jets is studied numerically using Eulerian framework for computation of steady flowfield and Lagrangian approach to computation of trajectories of particles carried by one of jets.

Computational experiments have shown that fast mixing in geometrical scale (in terms of the axial coordinate) does not necessarily mean rapid heat up (in temporal scale) of particles. Straightforward measures such as increasing hot-gas consumption, increasing the angle between hot and cold incident jets, and splitting the cold jet are not sufficient to achieve fast heating because of the behavior of particle trajectories.

To achieve rapid monotonic heating of particles carried by a central (cold) jet, the behavior of particle trajectories is studied. Three types of trajectories are observed. The particle trajectories can be bent either toward the interior of the cold jet (type 1) or outward (type 2). They also can rotate in the vortical zone upstream of the intersection of cold and hot jets (type 3). Direct exposure to the action of hot (peripheral) jets leads to the first or to the third type of trajectory behavior that causes slow or oscillating heating, respectively.

The proposed way to classify trajectories (pathlines) has been applied to optimization of reactor for production of carbon nanotubes (HiPco process). In the HiPco process, the catalyst particles carried by the central cold jet initialize formation of carbon nanotubes from carbon oxide. For the basic configuration of the HiPco reactor (one central and three peripheral jets), many trajectories are either of type 1 (for angle between jets $\alpha = 60$ deg) or type 3 (for $\alpha > 60$ deg). For smaller α, the type 2 trajectories provide steady, but slow heat up. The optimal angle between jets, $\alpha = 45$ deg, provides heating rate 1–1.5 deg $\times 10^5$ K/s for most of the trajectories considered at $T = 800$ K.

A modified reactor design, design C, has been proposed, which includes three parallel nozzles for cold central jets. To avoid direct exposure of trajectories to the action of hot jets, the cold-jet nozzles are located between the hot peripheral jet nozzles. Type 1 trajectories are avoided, and at the optimal angle between jets, $\alpha = 60$ deg, the heating rate reaches 3.5–4.5 deg $\times 10^5$ K/s, a significant improvement compared to the rate achieved by the basic design.

Acknowledgments

This research was supported by NASA under NASA Contract NAS1-97046 while the authors were in residence at ICASE, NASA Langley Research Center, Hampton, Virginia.

References

[1]Holdeman, J. D., Liscinsky, D. S., Oechsle, V. L., Samuelsen, G. S., and Smith, C. E., "Mixing of Multiple Jets with a Confined Subsonic Crossflow in a Cylindrical Duct," NASA TM 107185, 1996; also American Society of Mechanical Engineers, Paper ASME-96-GT-482, June 1996.

[2]Kim, S.-W., and Benson, T. J., "Fluid Flow of a Row of Jets in Crossflow—A Numerical Study," *AIAA Journal*, Vol. 31, 1993, pp. 806–813.

[3]Drummond, J. P., Carpenter, M. H., and Riggins, D. W., "Mixing and Mixing Enhancement in Supersonic Reacting Flowfields," *Progress in Asronautics and Aeronautics*, Vol. 137, 1991, pp. 383–455.

[4]Drummond, J. P., and Givi, P., "Suppression and Enhancement of Mixing in High-Speed Reacting Flow Field," *Combustion in High-Speed Flows*, edited by J. Buckmaster, Kluwer Academic, Dordrecht, The Netherlands, 1994, pp. 191–229.

[5]Povitsky, A., "Improving Jet Reactor Configuration for Production of Carbon Nanotubes," *Computers and Fluids*, Vol. 31, 2002, pp. 957–976; also preprint, ICASE Rept. 2000-18, 2000.

[6]Nikolaev, P., Bronikowski, M. J., Bradley, R. K., Rohmund, F., Colbert, D. T., Smith, K. A., and Smalley, R. E., "Gas-phase Catalytic Growth of Single-walled Carbon Nanotubes from Carbon Monoxide," *Chemical Physics Letters*, Vol. 313, 1999, pp. 91–97.

[7]Iijima, S., "Helical Microtubules of Graphitic Carbon," *Nature*, Vol. 354, 1991, pp. 56–58.

[8]Chico, L., Crespi, V. H., Benedict, L. X., Loui, S. G., and Cohen, M. L., "Pure Carbon Nanoscale Devices: Nanotube Heterojunctions," *Physical Review Letters*, Vol. 76, 1996, p. 76.

[9]Yu, M.-F., Files, B. S., Arepalli, S., and Ruoff, R. S., "Tensile Loading of Ropes of Single Wall Carbon Nanotubes and Their Mechanical Properties," *Physical Review Letters*, Vol. 84, 2000, pp. 5552–5555.

[10]Ajayan, P. M., Stephan, O., Redlich, P., and Colliex, C., "Carbon Nanotubes as Removable Templates for Metal Oxide Nanocomposites and Nanostructures," *Nature*, Vol. 375, 1995, p. 564.

[11]"FLUENT 6.1 User's Manual," Fluent, Inc., Lebanon, NH, 2000; URL: http://www.fluent.com [cited 22 September 2003].

[12]Bronikowski, M. J., Willis, P. A., Colbert, D. T., Smith, K. A., and Smalley, R. E., "Gas-phase Production of Carbon Single-Walled Nanotubes from Carbon Monoxide via the HiPco Process: A Parametric Study," *Journal of Vacuum Science and Technology*, Vol. A 19, No. 4, 2001, pp. 1800–1805.

[13]GAMBIT 1.2 User's Manual, Fluent Inc., Lebanon, NH, 2000; URL: http://www.fluent.com [cited 22 September 2003].

[14]Blacker, T. D., "The Cooper Tool," Proceedings of the 5th International Meshing Roundtable Conference, 1996, URL: http://www.imr.sandia.gov/ [cited 22 September 2003].

[15]Miyoshi, K., and Blacker, T.,"Hexahedral Mesh Generation Using Multi-Axis Cooper Algorithm," *Proceedings of the 9th International Meshing Roundtable Conference*, 2000, URL:http://www.imr.sandia.gov/ [cited 22 September 2003].

[16]Yakhot, V., and Orszag, S. A., "Renormalization Group Analysis of Turbulence: I. Basic Theory," *Journal of Scientific Computing*, Vol. 1, 1986, pp. 1–51.

[17]Yakhot, A., Orszag, S. A., Yakhot, V., and Israeli, M., "Renormalization Group Formulation of Large-Eddy Simulation," *Journal of Scientific Computing*, Vol. 4, 1989, pp. 139–158.

[18]Abramovich, G. N., *The Theory of Turbulent Jets*, MIT Press, Cambridge, MA, 1963.

[19]Weast, R. C., *CRC Handbook of Chemistry and Physics*, CRC Press, West Palm Beach, FL, 1977.

[20]Launder, B. E., and Spalding, D. B., "The Numerical Computation of Turbulent Flow," *Computer Methods in Applied Mechanics and Engineering*, Vol. 3, 1974, pp. 269–289.

[21]Patankar, S., *Numerical Heat Transfer and Fluid Flow*, Hemisphere, New York, 1980.

[22]Hirsch, C., *Numerical Computation of Internal and External Flows*, Vol. 1, *Fundamentals of Numerical Discretizations*, Wiley, New York, 1994.

[23]Issa, R. I., "Solution of Implicitly Discretized Fluid Flow Equations by Operator Splitting," *Journal of Computational Physics*, Vol. 62, 1986, pp. 40–65.

[24]Talbot, L., Cheng, R., Schefer, R., and Willis, D., "Thermophoresis of Particles in a Heated Boundary Layer," *Journal of Fluid Mechanics*, Vol. 101, No. 4, 1980, pp. 737–758.

I. Gökalp
Associate Editor